

One-Dimensional Electronic States in a Moiré Superlattice of Twisted Bilayer WTe₂

Takuto Kawakami,^{1,*} Hayato Tateishi,^{2,*} Daiki Yoshida,¹ Xiaohan Yang,³ Naoto Nakatsuji,⁴ Limi Chen,⁵ Kohei Aso,⁵ Yukiko Yamada-Takamura,⁵ Yoshifumi Oshima,⁵ Yijin Zhang,^{3,6} Tomoki Machida,³ Koichiro Kato,^{2,†} and Mikito Koshino^{1,‡}

¹*Department of Physics, Osaka University, Toyonaka, Osaka 560-0043, Japan*

²*Department of Applied chemistry, Kyushu University, Motoooka, Fukuoka 819-0395, Japan*

³*Institute of Industrial Science, The University of Tokyo, Tokyo 153-8505, Japan*

⁴*Department of Physics and Astronomy, Stony Brook University, Stony Brook, New York 11794, USA*

⁵*School of Materials Science, Japan Advanced Institute of Science and Technology, Ishikawa 923-1292, Japan*

⁶*Department of Physics, The University of Tokyo, Tokyo 113-0022, Japan*

(Dated: January 30, 2026)

One-dimensional (1D) moiré superlattices provide a new route to engineering reduced-dimensional electronic states in van der Waals materials, yet their electronic structure and microscopic origin remain largely unexplored. Here, we investigate the structural relaxation and electronic properties of a 1D moiré superlattice formed in twisted bilayer 1T'-WTe₂ using density functional theory calculations, complemented by high-angle annular dark-field scanning transmission electron microscopy. We show that lattice relaxation strongly reconstructs the moiré stripes, leading to stacking-dependent stripe widths that are in excellent agreement with experimental observations. The relaxed structure hosts quasi-one-dimensional electronic bands near the Fermi level, characterized by strong dispersion along the stripe direction and nearly flat dispersion in the perpendicular direction. By comparing the full bilayer with isolated relaxed layers, we establish that these 1D electronic states are governed predominantly by an intralayer moiré potential induced by in-plane lattice relaxation, rather than by interlayer hybridization. We extract this position-dependent moiré potential directly from DFT calculations and construct an effective tight-binding model that reproduces both the band dispersion and the real-space localization of the electronic wave functions. Our results identify lattice relaxation as the key mechanism underlying 1D electronic states in 1D moiré superlattices. The framework developed here provides a unified theoretical basis for realizing and exploring one-dimensional moiré physics in a broad class of anisotropic two-dimensional materials.

I. INTRODUCTION

Moiré superlattices in twisted two-dimensional (2D) materials have attracted considerable attention as a versatile platform for engineering electronic states [1–25]. The long-wavelength interference between two slightly mismatched lattices can strongly reconstruct the electronic band structure and give rise to a variety of novel topological and strongly correlated phases. In general, when two layers of the same 2D material are stacked with a small twist angle, the resulting moiré pattern can be regarded as a magnified and rotated image of the underlying atomic lattice. A representative example is twisted bilayer graphene, which hosts a two-dimensional moiré superlattice with sixfold rotational symmetry [4, 26]. Likewise, uniaxially anisotropic monolayers with reduced rotational symmetry give rise to an anisotropic two-dimensional moiré pattern in their low-angle twisted bilayers [27–31], as illustrated in Fig. 1(a).

In contrast, when anisotropic two-dimensional materials are stacked at specific large twist angles, the system can host a purely one-dimensional (1D) moiré superlattice, in which a given local stacking configuration extends

infinitely along a single direction [see Fig. 1(b)] [32, 33]. This situation arises when two inequivalent reciprocal lattice vectors of the monolayer are brought into exact alignment by twisting, as illustrated in the lower panel of Fig. 1(b), leaving only a single moiré reciprocal lattice vector [32]. Such 1D moiré superlattices have been experimentally observed in twisted bilayer 1T'-WTe₂ at twist angles near 60° [32] and in α - and β -Sb [34], and have been theoretically predicted in twisted bilayers of black phosphorene [35] and PdSe₂ [33]. Moreover, the emergence of a 1D moiré pattern via reciprocal-lattice coincidence can also be achieved by applying heterostrain [36–40].

The resulting structural anisotropy provides a promising platform for realizing 1D electronic phenomena [33, 35]. However, it remains an open question whether a 1D moiré pattern necessarily gives rise to intrinsically 1D electronic states. In this work, we perform density functional theory (DFT) calculations for the 1D moiré superlattice of twisted bilayer WTe₂ [32] and demonstrate the emergence of quasi-1D electronic states. In moiré systems, lattice relaxation is known to have a profound impact on the electronic band structure [41–49]. Here, we carry out a full structural optimization of the one-dimensional moiré superlattice and show that moiré stripes with different local stacking configurations develop uneven widths depending on their energetic stability. We further experimentally probe the atomic struc-

* These authors contributed equally to this work.

† Corresponding author: kato.koichiro.957@m.kyushu-u.ac.jp

‡ Corresponding author: koshino@phys.sci.osaka-u.ac.jp

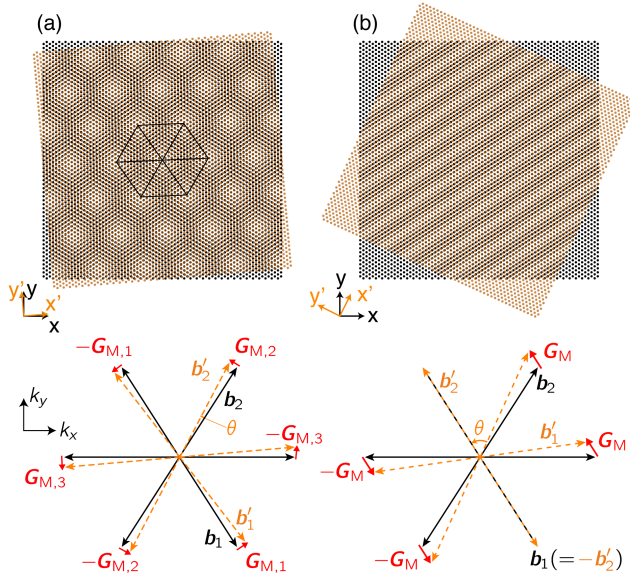


FIG. 1. Schematic illustration of a twisted bilayer composed of an anisotropic two-dimensional lattice stacked at (a) $\theta = 5^\circ$ and (b) $\theta \approx 65^\circ$. The anisotropic monolayer lattice is constructed by uniaxially deforming an equilateral triangular lattice by a factor of 0.9 along the x -direction of the unrotated configuration. While the low-angle stacking in (a) produces an anisotropic two-dimensional moiré pattern, the large-angle configuration in (b) gives rise to a purely one-dimensional moiré superlattice. The lower panels show the corresponding momentum-space constructions; in the one-dimensional case, only a single moiré reciprocal lattice vector \mathbf{G}_M remains.

ture of twisted bilayer WTe₂ at the corresponding twist angle using high-angle annular dark-field scanning transmission electron microscopy (HAADF-STEM), and confirm that the calculated atomic structure is in good agreement with the experimental images.

We then compute the electronic band structure of the optimized superlattice and demonstrate that the resulting bands exhibit a pronounced 1D character, with strong dispersion along the stripe direction and nearly flat dispersion in the perpendicular direction. Notably, we find that the formation of 1D bands is driven by in-plane lattice relaxation. Specifically, structural relaxation induces a position-dependent shear strain that generates an on-site moiré potential that varies periodically in the direction perpendicular to the moiré stripes. The 1D bands emerge as bound states localized near the extrema of this potential. We extract the moiré potential directly from DFT calculations of the locally distorted atomic structure and construct an effective tight-binding model incorporating this potential. The model successfully reproduces the essential features of the DFT band structure as well as the corresponding real-space wave functions.

We also introduce a general framework for constructing 1D moiré patterns, which is employed throughout this work. Specifically, we replace the original atomic structure of monolayer WTe₂ with an effective anisotropic

triangular lattice. Within this description, the emergence of a 1D moiré pattern can be readily understood from the slight shape mismatch between the rotated triangular lattices of the two layers. This real-space picture is complementary to the reciprocal-space construction discussed above [32]. Although our analysis focuses on 1T' transition-metal dichalcogenides (TMDCs), the method is broadly applicable to other systems exhibiting 1D moiré patterns. The general theoretical framework proposed here—combining one-dimensional moiré construction, lattice relaxation, and electronic structure analysis—is applicable to a broad class of anisotropic two-dimensional materials hosting one-dimensional moiré superlattices.

The remainder of this paper is organized as follows. In Sec. II, we introduce a general framework for constructing one-dimensional moiré patterns and describe the geometry of the 1D moiré superlattice in twisted bilayer WTe₂. In Sec. III, we determine the relaxed atomic structure using DFT calculations and compare the results with experimental observations. Section IV discusses the resulting electronic band structure and presents an effective tight-binding model that captures its essential features. Finally, Sec. V summarizes our findings.

II. 1D MOIRÉ PATTERN

A. Atomic structure

We first describe the atomic structure of a single 1T'-WTe₂ layer [50–68], which serves as the basis for constructing the moiré pattern in the twisted bilayer system. Figure 2 shows its crystal structure. Black dots represent W atoms, while red and blue dots represent Te atoms located above and below the W plane, respec-

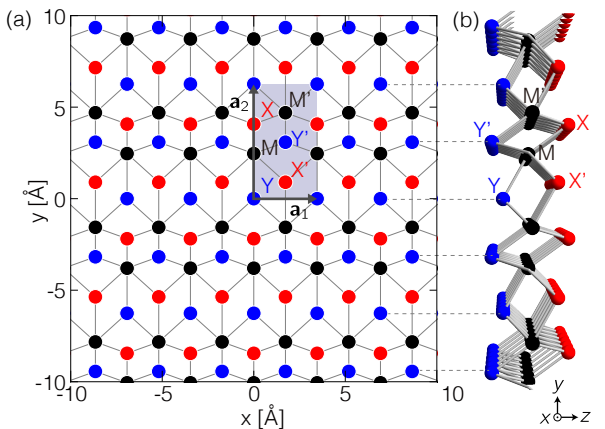


FIG. 2. Atomic structure of a 1T'-WTe₂ monolayer. (a) Top view of the in-plane structure. (b) Side view in the y - z plane. Black dots denote W atoms, while blue and red dots denote Te atoms. The shaded rectangle indicates the unit cell spanned by the primitive lattice vectors \mathbf{a}_1 and \mathbf{a}_2 .

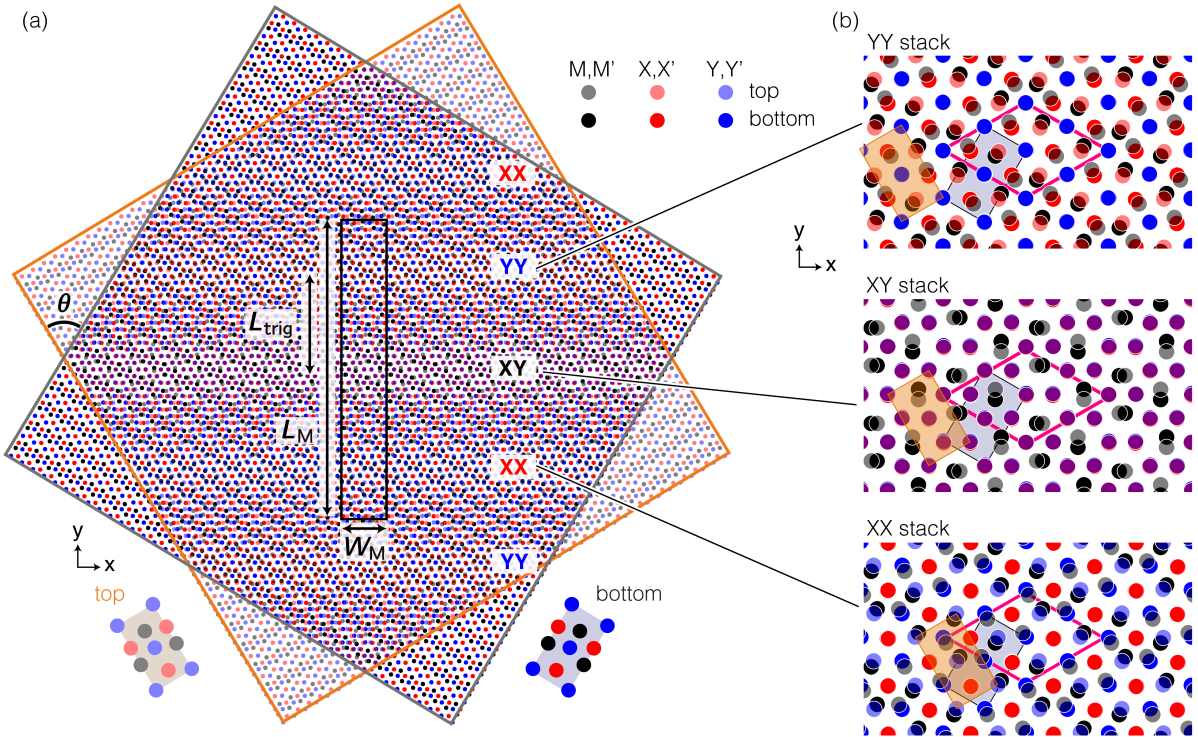


FIG. 3. (a) One-dimensional moiré pattern formed by twisting two 1T'-WTe₂ monolayers. The top layer (transparent dots) is rotated by $\theta \approx 62^\circ$ relative to the bottom layer (solid dots). (b) Periodic stacking configuration corresponding to the local structure in (a), with the period indicated by the rhombus. Periodic interlayer sliding along the x direction gives rise to the repeating XX, XY, and YY stacking configurations.

tively. The in-plane structure, shown in Fig. 2(a), has a rectangular unit cell containing six atoms: two W atoms (labeled M and M'), two Te atoms above the W plane (X and X'), and two Te atoms below the W plane (Y and Y'). The in-plane lattice constants are $|\mathbf{a}_1| \approx 3.46$ Å and $|\mathbf{a}_2| \approx 6.26$ Å, with directions $\mathbf{a}_1 \parallel \hat{x}$ and $\mathbf{a}_2 \parallel \hat{y}$. This structure belongs to the layer group $P2_1/m11$, generated by mirror reflection about the yz -plane and screw operation along the x -direction.

We now consider a twisted bilayer 1T'-WTe₂, where the top and bottom layers are rotated by $\pm\theta/2$. Figure 3(a) illustrate the atomic configuration for a twist angle of $\theta \sim 62^\circ$. We observe a one-dimensional moiré pattern, with the horizontal bright stripes indicating 1D moiré domains [32]. The local regions can be approximated as periodic stacking configurations, denoted as XX, XY, and YY, as shown in Fig. 3(b); their precise definitions are provided in the following section. This classification is analogous to the AA, AB, and BA stackings commonly used for twisted bilayer graphene. In the XY stacking, upper Te sites (X or X') in one layer are vertically aligned with lower Te sites (Y or Y') in the other layer. The XX and YY stackings are defined analogously.

B. Origin of the 1D moiré pattern

The formation of the 1D moiré pattern in WTe₂ can be understood using the concept of an effective triangular lattice, introduced from a momentum-space perspective [32]. Here we develop a complementary real-space description that provides an intuitive understanding of the 1D moiré structure in twisted bilayer 1T'-WTe₂.

The effective triangular lattice, shown by the solid lines in Fig. 4(a), is defined as a triangular grid commensurate with the monolayer unit cell of 1T'-WTe₂, where each vertex corresponds approximately to an atomic site of 1T'-WTe₂. The primitive lattice vectors of this effective lattice are given by

$$\boldsymbol{\tau}_1 = \mathbf{a}_1/2 - \mathbf{a}_2/6 \quad (1)$$

$$\boldsymbol{\tau}_2 = \mathbf{a}_1/2 + \mathbf{a}_2/6. \quad (2)$$

For each triangle plaquette, the mirror-reflection symmetry of the original monolayer enforces equal edge lengths, $|\boldsymbol{\tau}_1| = |\boldsymbol{\tau}_2| = \tau$, while the deviation from an equilateral triangle ($|\boldsymbol{\tau}_1 - \boldsymbol{\tau}_2| \neq \tau$) reflects the absence of threefold rotational symmetry in the 1T' structure. The relative two-dimensional position of the effective lattice with respect to the original lattice is arbitrary; for definiteness, we fix it such that the inversion center of the atomic structure (the midpoint between the X and Y' sites) coincides with the midpoint of an edge of the triangular

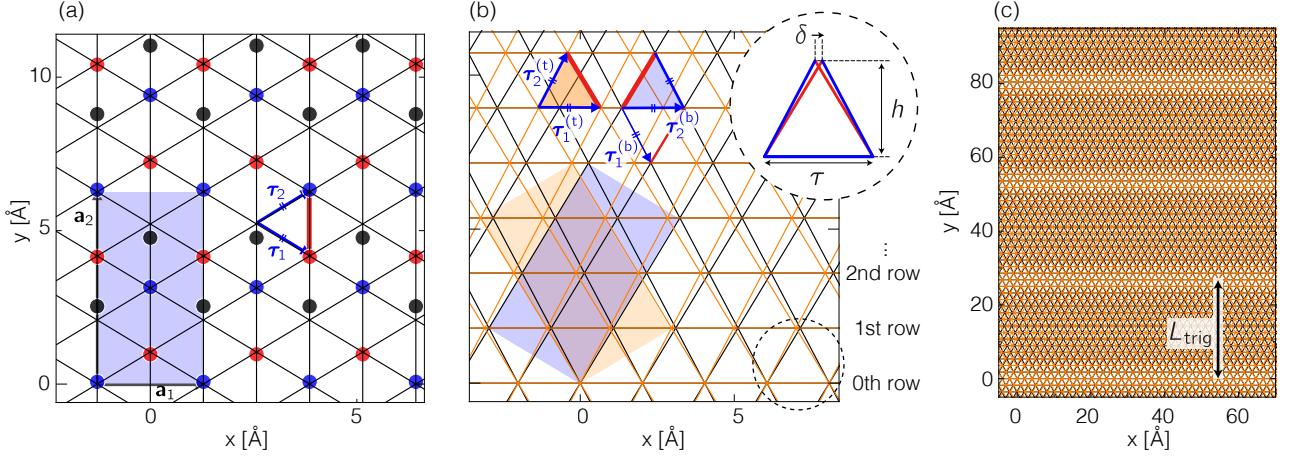


FIG. 4. (a) Effective isoscales triangular lattice approximating the atomic structure of WTe₂. (b) Twisted stacking of the effective triangular lattices. Black and orange denotes the bottom and top layers, respectively. The two layers are rotated such that their lattice vectors parallel to the x axis have the equal length but are not identical. The inset shows a magnified view of a single isoscales plaquette with an aligned baseline. (c) Zoom-out view of (b), showing a clear moiré period L_{trig} . Atomic color codes are the same as in Fig. 2

lattice.

We consider a twisted bilayer of this triangular lattice, obtained by rotating the top and bottom layers by $\pm\theta/2$, respectively. The rotated lattice vectors are denoted as $\tau_i^{(l)}$ with $l = t, b$ for the top and bottom layers. When θ is chosen as the relative angle between τ_1 and τ_2 , the configuration shown in Fig. 4(b) is realized, in which $\tau_1^{(t)}$ and $\tau_2^{(b)}$ coincide along the \hat{x} direction. In this arrangement, a one-dimensional moiré pattern naturally emerges. Let $y = 0$ denote the baseline, where the horizontal edges of the top and bottom triangular lattices coincide, defining a reference row [Fig. 4(b)]. In the first row above, the vertices are laterally shifted by a small amount δ along x , due to the non-equilateral geometry of the triangles, as shown in the inset of Fig. 4(b). As the structure repeats row by row, the displacement accumulates as $N\delta$ in the N -th row. When the accumulated shift satisfies $N\delta \simeq \tau$, the vertices realign, giving rise to a 1D moiré period [Fig. 4(c)]. The corresponding moiré wavelength is then

$$L_{\text{trig}} = Nh \simeq \frac{\tau h}{\delta}, \quad (3)$$

where h is the height of the triangles in y -direction (see Fig. 4(b), inset).

The bright stripes observed in twisted bilayer of 1T'-WTe₂ [Fig. 3(a)] corresponds to the 1D moiré pattern in the effective triangular lattice. However, these stripes do not share the same atomic arrangement; instead, the three distinct stacking patterns, XX, XY, and YY appear periodically, as discussed above. Therefore, the true moiré period is given by

$$L_M = 3L_{\text{trig}}. \quad (4)$$

This structural variation arises because the vertices of

the effective triangular lattice correspond to different atomic species in the underlying WTe₂ lattice. The periodic stacking structures for XX, XY, and YY, shown in Fig. 3(b), are defined by linearly transforming the WTe₂ lattice so that its effective lattice becomes an equilateral triangular lattice, and then overlapping a pair of such layers with a twist angle of 60°. The resulting structure possesses a translational symmetry, with the unit cell indicated by the pink rhombus in Fig. 3(b), and the different stacking types (XX, XY, YY) correspond to different lateral shifts between the two layers. In the original moiré twisted bilayer shown in Fig. 3(a), a movement of length L_{trig} along the y -direction corresponds to a horizontal interlayer shift by one triangle side (τ) in the commensurate bilayer. It can be shown that the stacking sequence of the commensurate bilayer changes periodically as XX, XY, YY, ... for each shift by τ , which explains the evolution of the local stacking structures in the moiré bilayer along the y -direction.

C. Commensurate approximant

Although the long-range moiré pattern can be described as above, the overall structure is not strictly periodic, due to the moiré period L_M is not generally commensurate with the underlying WTe₂ lattice. To obtain a commensurate structure, we slightly deform the effective triangular lattice so that its vertices realign exactly at $N = \lfloor \tau/\delta \rfloor$ row, where $\lfloor x \rfloor$ denote the nearest integer to x . To preserve the lattice symmetry, we apply a uniaxial isochoric strain to the unrotated effective lattice, transforming τ_i as

$$\tilde{\tau}_i = \begin{pmatrix} 1 + \varepsilon & 0 \\ 0 & (1 + \varepsilon)^{-1} \end{pmatrix} \tau_i, \quad (5)$$

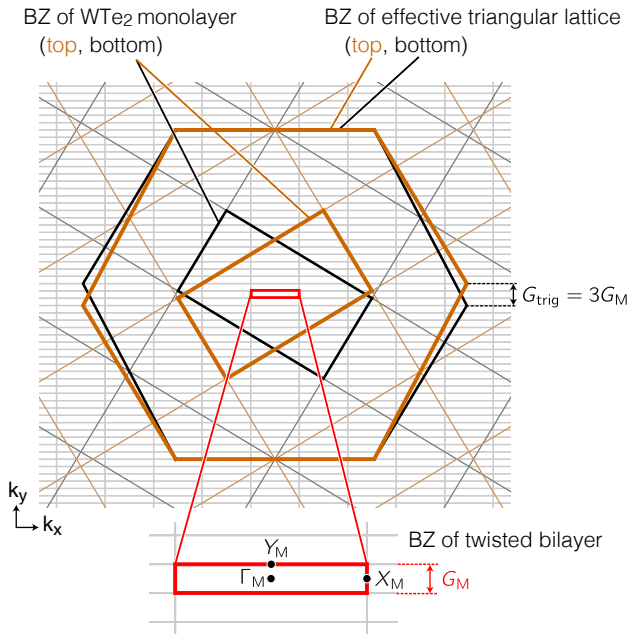


FIG. 5. Momentum-space structure of twisted bilayer WTe₂ for a commensurate approximant. Three levels of Brillouin zones are indicated, corresponding to the effective triangular lattice, the WTe₂ monolayers, and the commensurate bilayer supercell.

where ε is determined to satisfy the condition $\tilde{\tau}/\tilde{\delta} = \lfloor \tau/\delta \rfloor = N$. Here, a tilde denotes the quantity in the commensurately adjusted system. From geometric considerations, the required strain magnitude is

$$1 + \varepsilon = \sqrt{\frac{|\tau_1 - \tau_2|}{|\tau_1 + \tau_2|}} \left(\frac{3N - 1}{N + 1} \right)^{1/4}. \quad (6)$$

For WTe₂, we obtain $N = 15$, and $\varepsilon \approx 3.8 \times 10^{-5}$, using $\tau \approx 2.02$ Å and $\delta \approx 0.135$ Å. This deformation is sufficiently small that it does not significantly affect the electronic structure. Single-layer DFT calculations show that the resulting band shifts are approximately 1 meV. The resulting moiré period is $L_{\text{trig}} = N\tilde{h} \approx 26.8$ Å, and $L_M = 3L_{\text{trig}} \approx 80.4$ Å.

Using the adjusted lattice, the moiré superlattice vectors are defined to satisfy

$$\begin{aligned} \mathbf{a}_{M,i} &= R(\theta/2)(m_{i1}\tilde{\mathbf{a}}_1 + m_{i2}\tilde{\mathbf{a}}_2) \\ &= R(-\theta/2)(n_{i1}\tilde{\mathbf{a}}_1 + n_{i2}\tilde{\mathbf{a}}_2). \end{aligned} \quad (7)$$

The smallest integer solutions for the linearly independent $\mathbf{a}_{M,i}$ are $(m_{11}, m_{12}, n_{11}, n_{12}) = (12, 11, -12, 11)$ and $(m_{21}, m_{22}, n_{21}, n_{22}) = (-3, 1, -3, -1)$, which yield the moiré lattice constants

$$\mathbf{a}_{M,1} = L_M \hat{\mathbf{e}}_y \quad (8)$$

$$\mathbf{a}_{M,2} = -W_M \hat{\mathbf{e}}_x \quad (9)$$

with $L_M = 3L_{\text{trig}}$ and $W_M = 6\tilde{\tau}$. The unit cell spanned by $\mathbf{a}_{M,1}$ and $\mathbf{a}_{M,2}$ is shown a rectangle in Fig. 3(a). We

adopt this commensurate lattice to simulate the lattice relaxation and the electronic properties in Sec. III and IV.

Figure 5 illustrates the construction of the Brillouin zone (BZ) of the twisted bilayer system considered here. The brown and black rectangles denote the BZs of the top and bottom WTe₂ monolayers, respectively, while the hexagons represent the BZs of the effective triangular lattice. The smallest red rectangle corresponds to the BZ of the moiré unit cell of the commensurate twisted bilayer system obtained above, with its extent along the y direction given by $G_M = 2\pi/L_M$. The distance between the closest corners of the hexagonal Brillouin zones of the top and bottom layers defines $G_{\text{trig}} = 2\pi/L_{\text{trig}}$, which is the reciprocal lattice vector associated with the moiré pattern of the effective triangular lattice (Fig. 4). Here $G_{\text{trig}} = 3G_M$, reflecting the relation $L_M = 3L_{\text{trig}}$.

III. STRUCTURAL RELAXATION

In this section, we investigate the lattice relaxation of twisted bilayer WTe₂. Starting from the commensurate approximant of the rigid twisted bilayer described in Sec. II C, we perform a full DFT structural optimization. We compare the calculated structures with HAADF-STEM measurements and demonstrate good agreement between theory and experiment.

A. DFT structural analysis

We performed density functional theory (DFT) calculations by mainly employing two computational packages: Vienna Ab initio Simulation Package (VASP) [69, 70] for structure optimization, OpenMX [71–73] for band calculation. The following calculations were conducted with Perdew-Burke-Ernzerhof (PBE) generalized approximation (GGA) [74] and DFT-D3 method of Grimme with zero-damping function [75]. The projector augmented-wave (PAW) method [76] was employed for the pseudopotentials in VASP calculations. Also, norm-conserving Vanderbilt pseudopotential [77] and variationally optimizing numerical atomic orbitals [73] were used in OpenMX calculations.

We first optimized the primitive unit cell of monolayer 1T'-WTe₂ to determine its in-plane lattice constants ($|\mathbf{a}_1|$ and $|\mathbf{a}_2|$). The calculations employed a plane-wave cutoff energy of 300 eV and a $4 \times 2 \times 1$ Monkhorst-Pack k -point mesh for Brillouin-zone sampling [78]. The out-of-plane lattice constant was fixed at $c = 20$ Å to suppress spurious interactions between periodic images. After full relaxation of the atomic positions, cell shape, and volume, we obtained optimized lattice constants of approximately $|\mathbf{a}_1| = 3.46$ Å and $|\mathbf{a}_2| = 6.26$ Å.

We then constructed a commensurate 1D moiré system by stacking two structure-optimized monolayers at

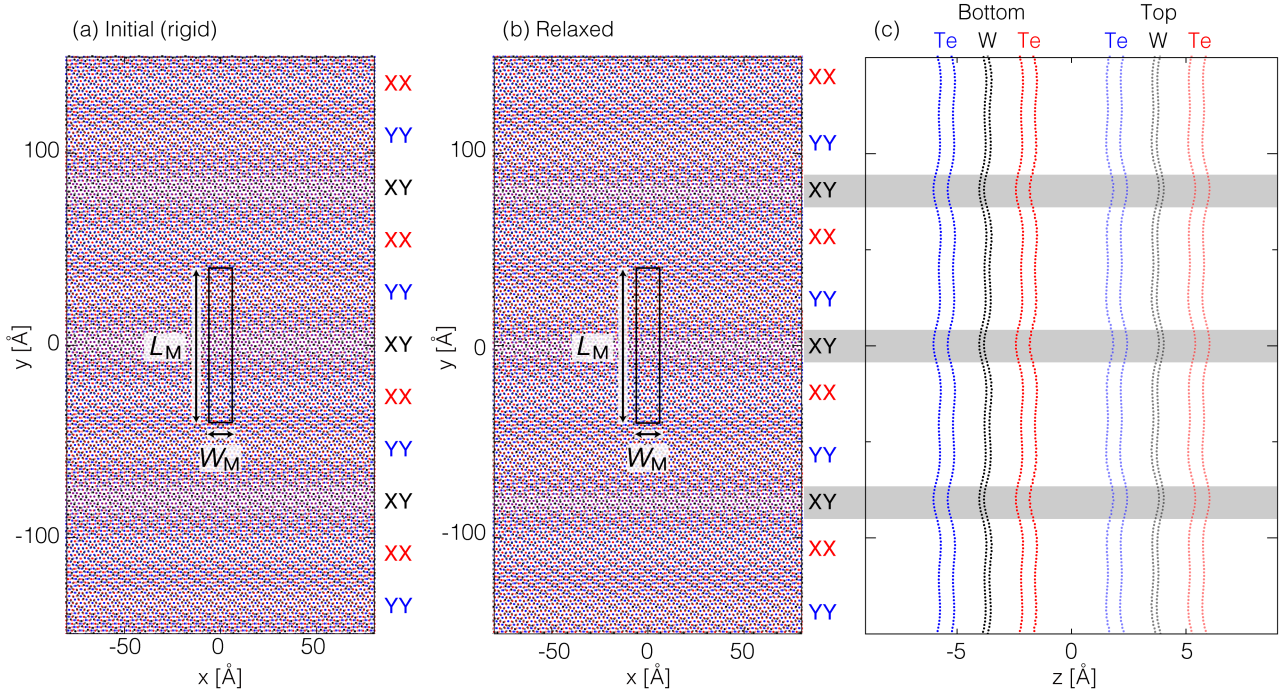


FIG. 6. DFT structural relaxation of twisted bilayer WTe₂. (a) Atomic structure of the rigid commensurate approximant before relaxation. The rectangle at the center denotes the unit cell. Multiple neighboring unit cells are shown for clarity. (b) Top view of the in-plane relaxed structure. The XY stacking stripe shrinks, while XX and YY stacking stripes broaden. (c) Side view of the relaxed structure with an enlarged z -axis scale. The interlayer distance increases in the XY stacking region. Atomic color codes are the same as those used in Figs. 2 and 3.

$\theta \approx 62^\circ$, following the commensuration procedure described in Sec. II C. The resulting configuration, shown in Fig. 6(a), is referred to as the rigid moiré structure. Starting from this structure, we performed a full structural optimization of the entire moiré supercell. In these calculations, the out-of-plane lattice constant was fixed at $c = 25$ Å, the plane-wave cutoff energy was set to 300 eV, and only the Γ point ($1 \times 1 \times 1$ k -point mesh) was used for Brillouin-zone sampling.

The optimized structure of the 1D moiré pattern, shown in Fig. 6(b), exhibits uneven stripe widths, with the XX and YY regions becoming significantly wider than the XY region. In general, moiré structures tend to suppress energetically unfavorable stacking configurations while expanding more stable ones, much like in graphene where the AA-stacked regions shrink and the AB/BA regions are enlarged [41, 42, 44]. In the present system, XY stacking is energetically unfavorable because the frontier Te atoms of the two layers approach each other too closely, resulting in excessive overlap of their filled out-of-plane p_z orbitals. This behavior is consistent with the well-known instability of chalcogen–chalcogen stacking in bilayer TMDC systems [79–81].

In contrast, the XX and YY stackings adopt an interlocking arrangement in which a convex Te atom from one layer fits into a concave region of the opposing layer. Consequently, the system spontaneously reduces the XY-stacked domains while expanding the XX and YY regions

through lateral atomic displacements. Figure 6(c) shows a side view of the atomic structure in the yz plane. We find that the interlayer Te–Te distance varies periodically along the moiré pattern, ranging from 3.04 to 3.68 Å. This variation is most pronounced in the XY-stacked regions, where the increased spacing reflects the near-contact configuration of the frontier Te atoms.

We also investigate the local lattice distortions associated with structural relaxation. For each monolayer unit cell in the relaxed twist bilayer [illustrated in Fig. 11(a) in a later section], we extract the local lattice vectors $\mathbf{a}_{i,\text{relax}}^{(l)}$ ($i = 1, 2$) for layer $l = t, b$ (top and bottom), and characterize the local lattice distortion following the standard strain-rotation decomposition [82].

$$\mathbf{a}_{i,\text{relax}}^{(l)} = \begin{pmatrix} 1 + \epsilon_{xx}^{(l)} & \epsilon_{xy}^{(l)} - \Omega^{(l)} \\ \epsilon_{xy}^{(l)} + \Omega^{(l)} & 1 + \epsilon_{yy}^{(l)} \end{pmatrix} \mathbf{a}_i^{(l)} \quad (10)$$

Here, $\mathbf{a}_i^{(l)} = R(\pm\theta/2)\mathbf{a}_i$ (\pm for $l = t, b$) denotes the intrinsic lattice vectors of monolayer WTe₂ without the relaxation, $\epsilon_{xx}^{(l)}$ and $\epsilon_{yy}^{(l)}$ represent the uniaxial strain components, $\epsilon_{xy}^{(l)}$ is the shear strain, and $\Omega^{(l)}$ corresponds to the local rotation. Figure 7 shows the spatial distribution of the lattice distortions. The upper panels display vector maps of the atomic displacements in each layer, while the lower panels present the corresponding profiles of the shear strain $\epsilon_{xy}^{(l)}$ as functions of the unit-cell center position along the y direction.

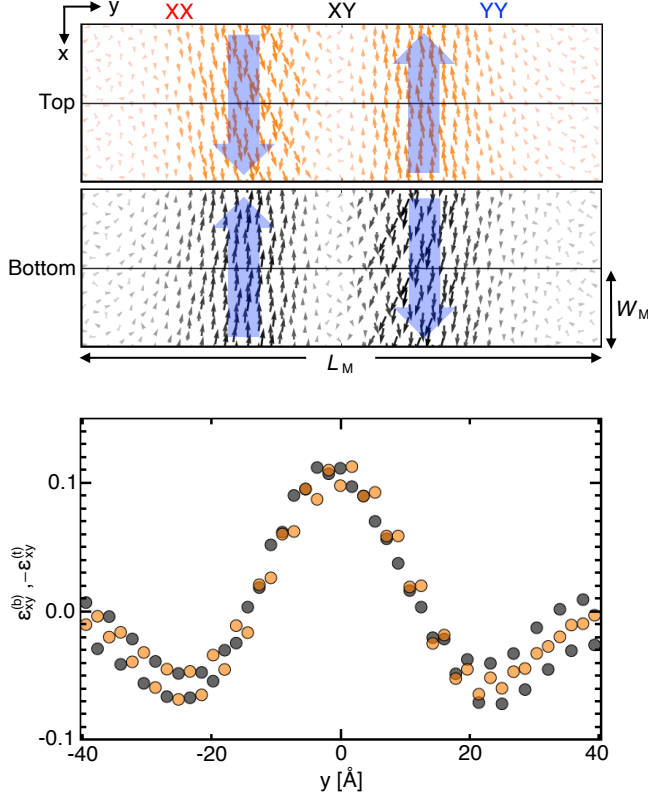


FIG. 7. (Top) Atomic displacements induced by lattice relaxation in top and bottom layers. The arrow lengths are scaled to be fourteen times the actual displacement amplitudes. Blue arrows schematically indicate the dominant displacement directions in each region. (Bottom) Shear strain components, $\epsilon_{xy}^{(b)}, -\epsilon_{xy}^{(t)}$, plotted as a function of the unit-cell center position along the y direction, perpendicular to the moiré stripes. Orange and black symbols denote the top and bottom layers, respectively.

In the vector maps, we observe relative interlayer sliding along the x axis (vertical direction in Fig. 7) on either side of the XY stacking region, with opposite sliding directions. This sliding motion is closely related to the narrowing of the XY stripe upon relaxation. Specifically, interlayer sliding along the x direction induces a shift of the moiré pattern along the y direction, as can be understood from the effective triangular-lattice picture shown in Fig. 4(b). The opposite sliding directions on the left- and right-hand sides of the XY region lead to moiré pattern shifts toward $\pm y$, resulting in a reduction of the XY domain width. Correspondingly, $\epsilon_{xy}^{(l)}$ exhibits pronounced peaks in the XY stacking region, originating from opposite atomic displacements along the x direction on either side of the region.

B. Experimental validation

We compare the DFT-optimized structure with the experimentally observed atomic arrangement of twisted bilayer 1T'-WTe₂, obtained using high-angle annular dark-field scanning transmission electron microscopy (HAADF-STEM) [32]. The van der Waals structure was made from mechanically exfoliated monolayer 1T'-WTe₂ by the dry transfer method. The twisted bilayer 1T'-WTe₂ was made from a single monolayer 1T'-WTe₂ using the tear-and-stack method which provides good control of twist angle. As WTe₂ is highly air-sensitive, mechanical exfoliation and van der Waals assembly were carried out in the glove box filled with dry nitrogen. The twisted bilayer were covered by ultrathin *h*-BN as a protective layer before taking out from the glove box. (Fig. 8(a)).

Figure 8(b) compares a HAADF-STEM image of a $\sim 62^\circ$ twisted-bilayer 1T'-WTe₂ with two simulated images of the rigid and DFT-optimized structures. The latter two images were obtained simply by rendering the structures in Figs. 6(a) and (b) in grayscale, respectively. Experimentally, we observed 1D moiré stripes running horizontally in the panel. Perpendicular to these stripes, the contrast alternates between relatively bright and dark stripes. The moiré period in our sample was 8.2 nm and includes three bright and three dark stripes per period (orange rectangle). The three bright stripes from top to bottom correspond to YY, XY and XX regions.

As reported previously [32], the characteristic atomic configurations within each stripe are already well reproduced by the rigid model. This agreement is not altered for the DFT-optimized structure Fig. 8(c). Furthermore, we find that the widths of the stripes, which were not discussed in earlier work, agree more closely with the simulation based on the DFT-optimized structure. This comparison is highlighted in the zoomed images in Fig. 8(d), which show a single moiré period for the rigid structure, the STEM image, and the DFT-optimized structure extracted from Figs. 8(b), respectively. The DFT relaxation reduces the extent of the XY region (orange shading) while expanding the XX and YY regions (blue shading). These trends closely match the experimentally observed atomic arrangement of twisted bilayer 1T'-WTe₂, supporting the validity of our DFT-based approach for modeling lattice relaxation in 1D moiré systems.

IV. ELECTRONIC BAND STRUCTURE

We analyze the electronic properties of the relaxed twisted bilayer WTe₂ obtained in Sec. III using DFT calculations. As shown below, the system exhibits a pronounced 1D electronic character: the low-energy bands are strongly dispersive along the moiré stripes while remaining nearly flat in the perpendicular direction. We further find that this anisotropy arises primarily from lattice relaxation, which generates an in-plane potential modulation. The resulting low-energy states can be inter-

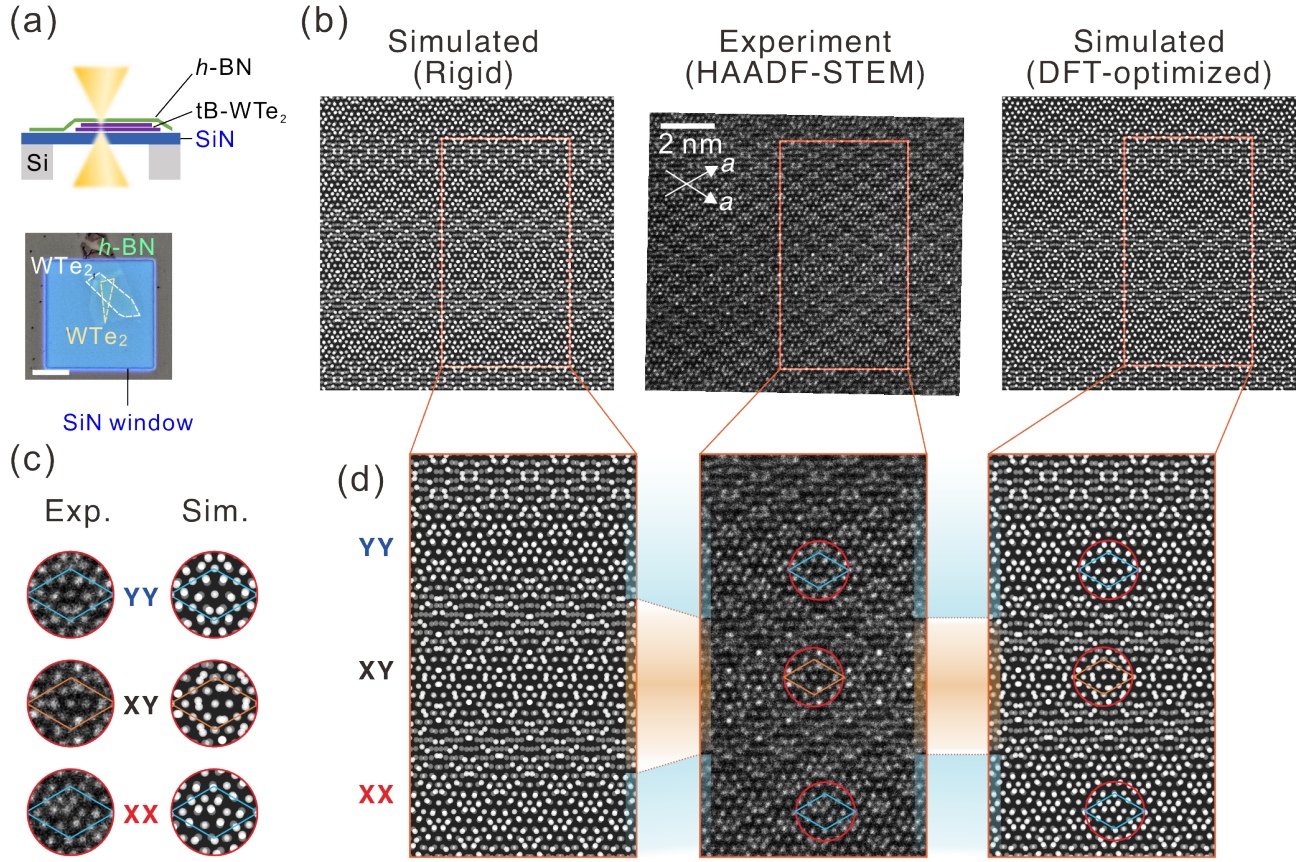


FIG. 8. (a) Schematic and optical micrograph of the sample. The white scale bar: 10 μ m. (b) Comparison of experimental HAADF-STEM image of 62.51° twisted bilayer 1T'-WTe₂ with simulated STEM images using (left) the rigid structure and (right) the DFT-optimized structure. (c) Atomic arrangements of three motifs. (d) Comparison of simulated STEM images with the experimental STEM image.

interpreted as confined modes within the moiré-induced potential landscape.

A. DFT band structure

We performed band calculations for the optimized commensurate 1D moiré unit cell. Charge density cut-off was set to 150 Ry, and Te7.0-s3p2d2f1 and W7.0-s3p2d2f1 were employed as pseudoatomic orbitals. Spin-orbit coupling was included self-consistently [83], and the Brillouin zone was sampled using a 1 \times 4 \times 1 grid of k points mesh.

The resulting band structure along the high-symmetry directions of the moiré Brillouin zone [Fig. 5] is presented in Fig. 9(a), where the zero of the energy axis is set at the Fermi energy. Figure 9(b) shows a three-dimensional plot of the band-energy surface for the region highlighted by the rectangle in Fig. 9(a). The bands near the valence-band maximum at the Γ_M point, labeled as groups I, II, and III, appear in fourfold groups. This reflects the two spin and two layer degrees of freedom, while the small splittings within each group arise from

interlayer hybridization and inversion-symmetry breaking introduced by the twist. Notably, the groups I is nearly flat along the Y_M - Γ_M direction (perpendicular to the moiré stripe), while showing significant dispersion along the Γ_M - X_M direction (parallel to the stripe). This anisotropic structure suggests suppressed electron motion across the moiré stripes and enhanced transport along them, indicating a 1D electronic character. The dispersion along the Y_M - Γ_M direction becomes progressively more pronounced for lower-energy groups (from I to III). We also find that the lowest conduction band, labeled as I' and II', exhibit a similar one-dimensional dispersion. The conduction band extends to lower energies and crosses the Fermi level, reflecting the semimetallic nature of monolayer WTe₂, where the lowest branch retains a quasi-one-dimensional character.

The one-dimensional character of the energy bands is also reflected in the electronic wave functions. Figure 9(c) shows the real-space distributions of the wave functions for groups I, II, and III (right three panels), obtained by summing the probability density over all states within each group. The leftmost panel shows the atomic configuration for reference. The wave function of

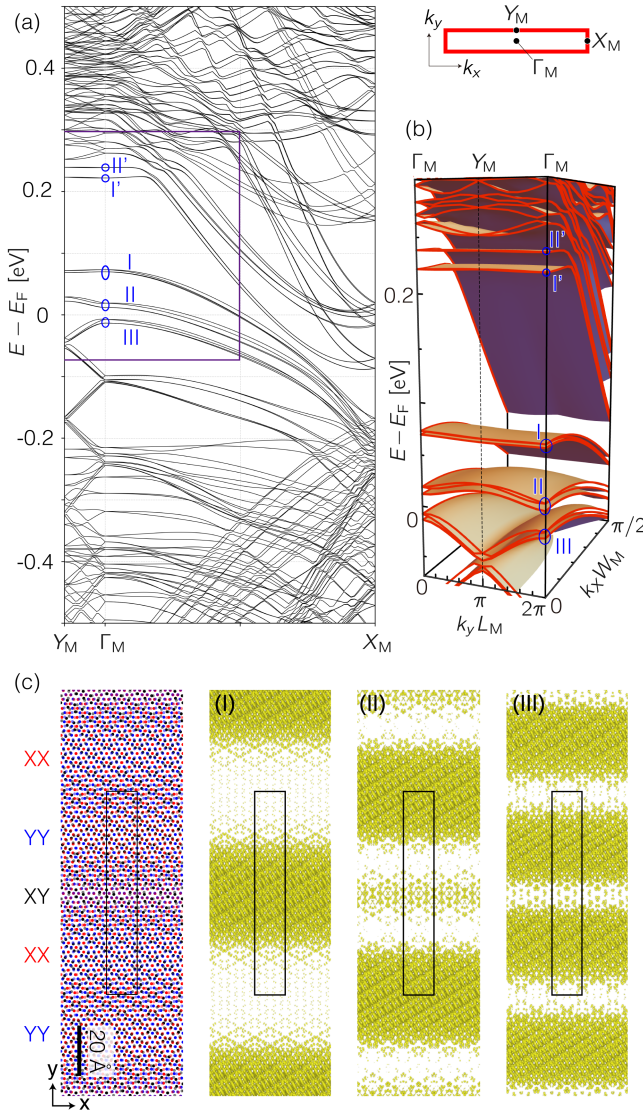


FIG. 9. DFT electronic states. (a) Electronic band structure of the moiré unit cell along the high symmetry paths in the moiré Brillouin zone (see also Fig. 5). (b) Three-dimensional band dispersion in the region enclosed by the purple line in (a). (c) From left to right: optimized 1D moiré structure, and real-space probability densities of the electronic states in group I, II, and III as indicated in the panels (a) and (b).

group I exhibits a pronounced stripe pattern, strongly localized around the XY stacking regions and separated by low-density areas, consistent with its 1D band structure, which disperses predominantly along the horizontal (x) direction. Groups II and III display similar stripe patterns but with increasing overlap between neighboring stripes, corresponding to their larger band dispersion along the perpendicular direction.

To disentangle the respective roles of interlayer coupling and intralayer moiré strain in shaping the 1D electronic structure, we performed DFT band calculations for an *isolated twisted bilayer*, in which the two layers

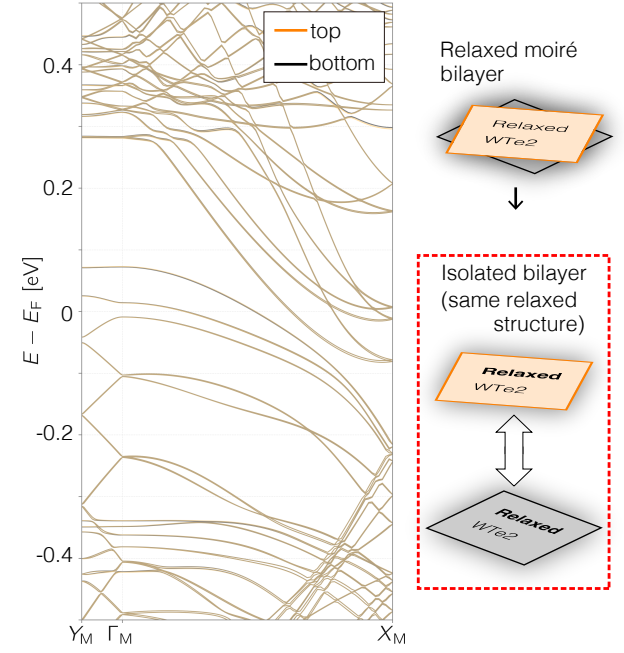


FIG. 10. Electronic bands calculated for isolated layers extracted from the structurally optimized moiré bilayer. The orange and black curves denote the top and bottom layers, respectively. The right panel shows a schematic illustration of isolated individual 1T'-WTe₂ layers under moiré-induced lattice relaxation.

are separated while each layer retains the atomic configuration of the fully relaxed moiré bilayer. As shown in Fig. 10, the resulting band structure, featuring nearly degenerate top and bottom layer bands, closely resembles that of the full bilayer [Fig. 9(a)], including its 1D character, apart from minor splittings attributable to interlayer hybridization. This observation indicates that the electronic structure near the Fermi level is governed predominantly by the intralayer moiré potential arising from lattice relaxation, rather than by interlayer coupling.

B. Effective tight-binding model

To elucidate the microscopic origin of the observed electronic features, we construct an effective tight-binding model that reproduces the DFT band structure. As shown in the previous section, the emergence of the one-dimensional character is dominated by intralayer effects, while interlayer hopping leads only to relatively small band splittings. Motivated by this observation, we assume that the essential qualitative features can be captured by a tight-binding model incorporating an intralayer on-site moiré potential induced by lattice relaxation within each layer.

The derivation of the moiré potential proceeds as follows. We divide the relaxed twisted bilayer into monolayer unit cells, as illustrated in Fig. 11(a), where the atomic configuration within each cell varies slightly from

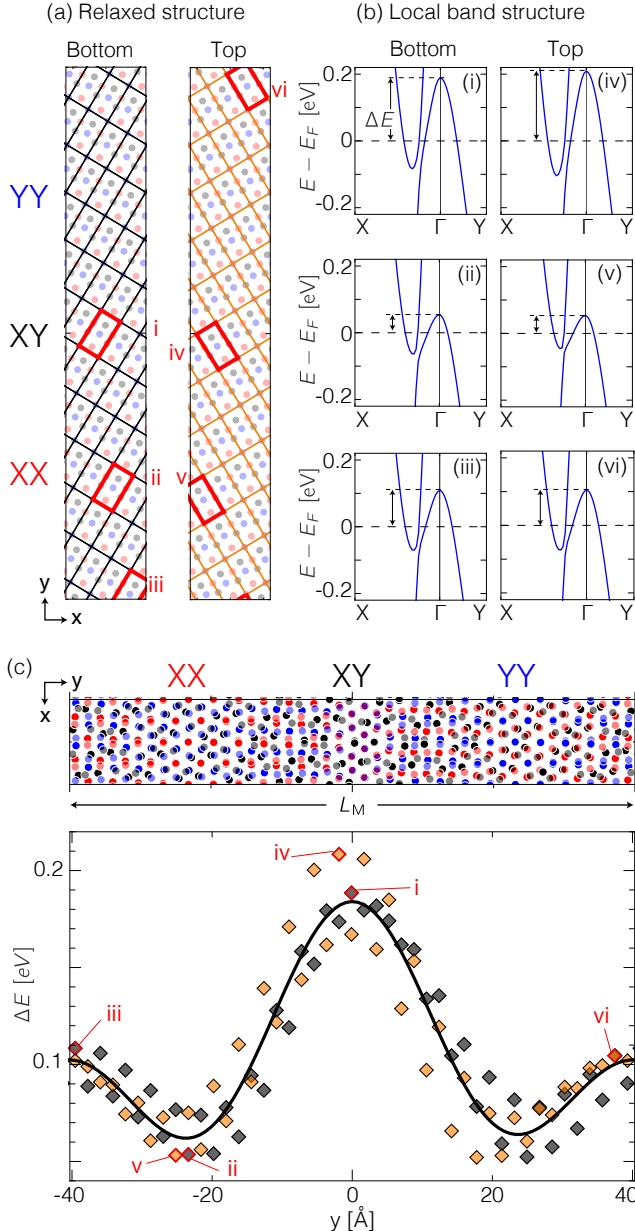


FIG. 11. Electronic bands associated with the local atomic structures. (a) atomic structure of the relaxed twisted bilayer WTe₂, with the two layers separated. Rectangles indicate local unit cells defined by connecting neighboring Y tellurium atoms (Fig. 2). The local unit cells and internal atomic configurations exhibit small but finite modulation across the moiré pattern. (b) Representative local band structures for unit cells labeled i-vi in panel (a). (c) Energy of the top of the hole-like band at Γ , relative to the Fermi energy, plotted as a function of unit-cell center position along the y direction, perpendicular to moiré stripes. Orange and black symbols denote the top and bottom layers, respectively.

place to place due to moiré-induced lattice distortions. For each unit cell, we perform a monolayer DFT calculation assuming periodic boundary conditions for that cell. The resulting band structures, shown in Fig. 11(b), exhibit a systematic dependence on position, reflecting the local variations in the atomic structure. We define the energy difference between the Fermi level and the valence-band maximum as ΔE , which serves as an effective local on-site potential for valence electrons.

Figure 11(c) plots ΔE as a function of the position of the unit-cell center projected onto the y direction. We find that ΔE varies nearly continuously across the moiré pattern, where the top and bottom layers exhibit nearly identical trends with maxima in the XY regions and minima in the XX and YY regions. The intralayer moiré potential V_{eff} is then obtained by fitting all ΔE data points from both layers to a single function of the following form:

$$V_{\text{eff}}(\mathbf{r}) = V_0 + V_1 \cos(\mathbf{G}_M \cdot \mathbf{r} + \varphi_1) + V_2 \cos(2\mathbf{G}_M \cdot \mathbf{r} + \varphi_2),$$

where $\mathbf{G}_M = G_M \mathbf{e}_y$ is the moiré reciprocal lattice vector. The fitting parameters are obtained as $V_0 \approx 0.106$ eV, $V_1 \approx 0.0408$ eV, $V_2 \approx 0.0374$ eV, $\varphi_1 \approx -0.0192$ rad, $\varphi_2 \approx 0.0105$ rad. The inclusion of the second harmonic term reflects the anharmonic shape of the moiré potential, while the small phase shifts φ_1 and φ_2 indicate that the potential minima are nearly aligned with the high-symmetry stacking positions. Notably, the spatial profile of the effective moiré potential closely resembles that of $\epsilon_{xy}^{(I)}$ shown in Fig. 7, indicating that the intralayer moiré potential arises predominantly from shear strain induced by lattice relaxation.

The effective tight-binding model is constructed by incorporating this moiré potential into the tight-binding Hamiltonian. All monolayer unit cells are assumed to share identical hopping parameters, which are obtained from DFT calculations of the intrinsic, undistorted WTe₂ monolayer. We employ the $\{d_{xy}, d_{yz}, d_{zx}, d_{x^2-y^2}, d_{z^2}\}$ orbitals of W and the $\{p_x, p_y, p_z\}$ orbitals of Te as the basis set. By adding the position-dependent on-site potential $V_{\text{eff}}(\mathbf{r})$ to all the atomic sites, the effective tight-binding model is fully specified.

Figure 12 presents the band structures obtained from the tight-binding model: (a) without and (b) with the effective moiré potential. In panel (b), pronounced one-dimensional features emerge near the valence-band maximum along the $Y_M-\Gamma_M$ direction, in good agreement with the DFT results shown in Fig. 9, apart from the small splittings induced by interlayer coupling, which are absent in the effective model. The wave functions at the Γ_M point, shown in Fig. 12(c), also exhibit a one-dimensional spatial distribution aligned with the stripe pattern, consistent with the DFT wave-function profiles in Fig. 9(c). By comparison with the spatial profile of the effective potential V_{eff} , we interpret the group-I and group-III states as the ground and second excited bound states, respectively, of holes confined near the potential maxima at the XY regions. The group-II states correspond to bound states associated with the secondary potential maxima

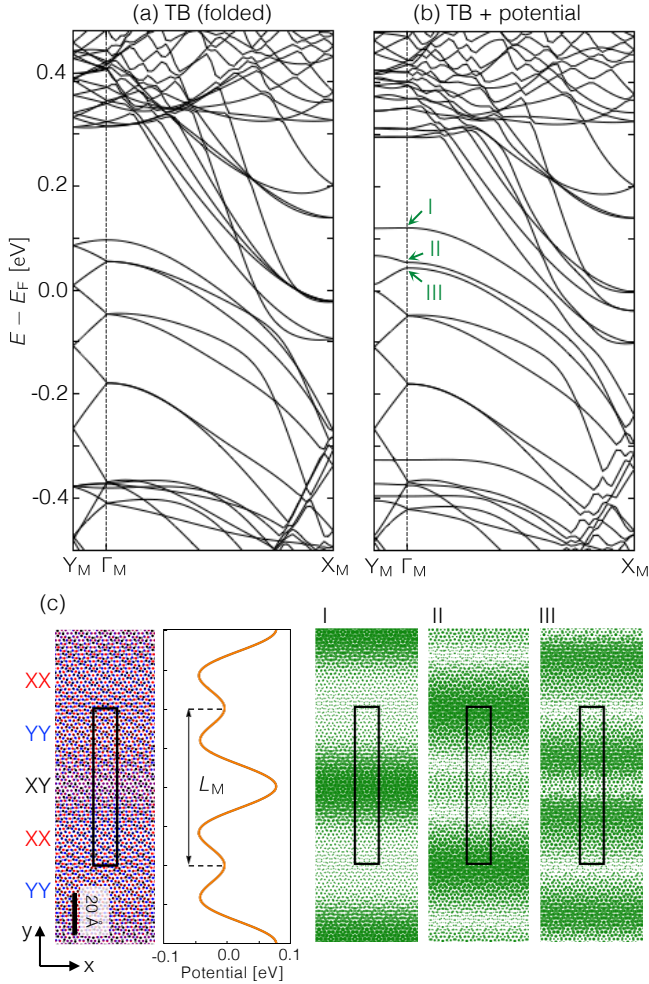


FIG. 12. Band structure of the effective tight-binding model. (a) Electronic structure of single-layer WTe₂ folded into the moiré Brillouin zone. (b) Band structure including the potential induced by lattice relaxation. (c) spatial modulation of the potential, taken from the Γ -point energy variation in Fig. 11, together with the wave-function amplitudes of states I-III indicated in panel (b)

at the XX and YY regions. From these considerations, we conclude that the emergence of one-dimensional energy bands near the Fermi level in twisted bilayer WTe₂ is primarily driven by the intralayer moiré potential induced by lattice relaxation.

V. CONCLUSION

We have investigated the structural relaxation and electronic properties of a one-dimensional moiré superlattice formed in twisted bilayer 1T'-WTe₂. Using first-principles DFT calculations, supported by high-resolution HAADF-STEM measurements, we showed that lattice relaxation strongly reconstructs the moiré stripes, leading to stacking-dependent stripe widths in

quantitative agreement with experiment. The relaxed structure hosts one-dimensional electronic bands near the Fermi level, characterized by strong dispersion along the stripe direction and weak dispersion in the perpendicular direction.

By disentangling interlayer and intralayer effects, we established that these 1D electronic states originate predominantly from an intralayer moiré potential induced by in-plane lattice relaxation. An effective tight-binding model incorporating this position-dependent potential successfully reproduces the DFT band structure and wave-function localization. Our results identify lattice relaxation as the key mechanism underlying one-dimensional electronic states in 1D moiré superlattices, and highlight twisted bilayer WTe₂ as a promising platform for exploring emergent one-dimensional moiré physics.

Unlike previously studied one-dimensional systems such as nanotubes or quantum wires, the 1D moiré superlattice naturally realizes an extended array of parallel one-dimensional channels with uniform geometry and tunable parameters inherited from the parent two-dimensional material. The simultaneous presence of many equivalent 1D channels is expected to substantially enhance one-dimensional signatures compared to isolated or sample-dependent realizations, providing a robust platform for exploring one-dimensional many-body physics—such as Tomonaga–Luttinger liquid behavior and other interaction-driven phenomena—as well as collective states emerging from coupled one-dimensional channels. In the present system, the one-dimensional valence-band channels intersect the conduction bands at the Fermi level, reflecting the intrinsic semimetallic nature of monolayer 1T'-WTe₂. This band overlap may influence the manifestation of one-dimensional many-body physics through additional screening or interband coupling effects. In contrast, semiconducting anisotropic materials, where such band overlap is absent, are expected to provide a cleaner realization of isolated one-dimensional moiré channels. Exploring these systems therefore represents an important direction for future studies of one-dimensional moiré physics.

The general construction method for one-dimensional moiré patterns based on an effective anisotropic triangular lattice, which is adopted throughout this paper, predicts the emergence of 1D moiré superlattices in a wide class of anisotropic two-dimensional materials, including twisted bilayers of black phosphorene [35] and PdSe₂ [33], as well as other low-symmetry transition-metal dichalcogenides. The theoretical approach presented here—including the one-dimensional moiré description, structural optimization, and electronic band analysis—provides a unified framework for exploring one-dimensional moiré physics across a broad range of materials beyond twisted bilayer WTe₂.

ACKNOWLEDGMENTS

This work was supported by JSPS KAKENHI (Grants Nos. JP21H05232, JP21H05234, JP21H05236, JP22K18317, JP24K01293, JP24K06921, JP24K06921, JP24K21195, JP25H00602, JP25K00938); JST-CREST and JST-PRESTO (Grant Nos. JPMJCR20T3, JP-MJCR20B4, JPMJPR24H8); Advanced Research Infrastructure for Materials and Nanotechnology in Japan

(ARIM), MEXT (Grant Numbers JPMXP1223JI0033, JPMXP1224JI0026); JSPS Overseas Research Fellowship; JST SPRING (Grant Nos. JPMJSP2108, JP-MJSP2102); the World-Leading Innovative Graduate Study Program for Advanced Basic Science Course at the University of Tokyo. The DFT calculations were carried out using the computer resource offered under the category of General Projects by Research Institute for Information Technology, Kyushu University.

[1] E. Y. Andrei and A. H. MacDonald, Graphene bilayers with a twist, *Nature materials* **19**, 1265 (2020).

[2] S. J. Shah, J. Chen, X. Xie, X. Oyang, F. Ouyang, Z. Liu, J.-T. Wang, J. He, and Y. Liu, Progress and prospects of moiré superlattices in twisted tmd heterostructures, *Nano Research* **17**, 10134 (2024).

[3] S. Gupta, J.-J. Zhang, J. Lei, H. Yu, M. Liu, X. Zou, and B. I. Yakobson, Two-dimensional transition metal dichalcogenides: A theory and simulation perspective, *Chemical Reviews* **125**, 786 (2025).

[4] J. Lopes dos Santos, N. Peres, and A. Castro Neto, Graphene bilayer with a twist: Electronic structure, *Phys. Rev. Lett.* **99**, 256802 (2007).

[5] E. Suárez Morell, J. D. Correa, P. Vargas, M. Pacheco, and Z. Barticevic, Flat bands in slightly twisted bilayer graphene: Tight-binding calculations, *Phys. Rev. B* **82**, 121407 (2010).

[6] R. Bistritzer and A. H. MacDonald, Transport between twisted graphene layers, *Phys. Rev. B* **81**, 245412 (2010).

[7] R. Bistritzer and A. MacDonald, Moiré bands in twisted double-layer graphene, *Proc. Natl. Acad. Sci.* **108**, 12233 (2011).

[8] P. Moon and M. Koshino, Energy spectrum and quantum hall effect in twisted bilayer graphene, *Phys. Rev. B* **85**, 195458 (2012).

[9] C.-C. Lu, Y.-C. Lin, Z. Liu, C.-H. Yeh, K. Suenaga, and P.-W. Chiu, Twisting bilayer graphene superlattices, *ACS Nano* **7**, 2587 (2013), pMID: 23448165.

[10] C. R. Dean, L. Wang, P. Maher, C. Forsythe, F. Ghahari, Y. Gao, J. Katoch, M. Ishigami, P. Moon, M. Koshino, *et al.*, Hofstadter's butterfly and the fractal quantum hall effect in moiré superlattices, *Nature* **497**, 598 (2013).

[11] Y. Cao, V. Fatemi, A. Demir, S. Fang, S. L. Tomarken, J. Y. Luo, J. D. Sanchez-Yamagishi, K. Watanabe, T. Taniguchi, E. Kaxiras, R. C. Ashoori, and P. Jarillo-Herrero, Correlated insulator behaviour at half-filling in magic-angle graphene superlattices, *Nature* **556**, 80 (2018).

[12] Y. Cao, V. Fatemi, S. Fang, K. Watanabe, T. Taniguchi, E. Kaxiras, and P. Jarillo-Herrero, Unconventional superconductivity in magic-angle graphene superlattices, *Nature* **556**, 43 (2018).

[13] S. Huang, K. Kim, D. K. Efimkin, T. Lovorn, T. Taniguchi, K. Watanabe, A. H. MacDonald, E. Tutuc, and B. J. LeRoy, Topologically protected helical states in minimally twisted bilayer graphene, *Phys. Rev. Lett.* **121**, 037702 (2018).

[14] M. Koshino, N. F. Q. Yuan, T. Koretsune, M. Ochi, K. Kuroki, and L. Fu, Maximally localized wannier orbitals and the extended hubbard model for twisted bilayer graphene, *Phys. Rev. X* **8**, 031087 (2018).

[15] M. Yankowitz, S. Chen, H. Polshyn, Y. Zhang, K. Watanabe, T. Taniguchi, D. Graf, A. F. Young, and C. R. Dean, Tuning superconductivity in twisted bilayer graphene, *Science* **363**, 1059 (2019).

[16] F. Wu, T. Lovorn, E. Tutuc, I. Martin, and A. H. MacDonald, Topological insulators in twisted transition metal dichalcogenide homobilayers, *Phys. Rev. Lett.* **122**, 086402 (2019).

[17] H. Yu, M. Chen, and W. Yao, Giant magnetic field from moiré induced berry phase in homobilayer semiconductors, *National Science Review* **7**, 12 (2019).

[18] S. Carr, S. Fang, and E. Kaxiras, Electronic-structure methods for twisted moiré layers, *Nature Reviews Materials* **5**, 748 (2020).

[19] K. Yasuda, X. Wang, K. Watanabe, T. Taniguchi, and P. Jarillo-Herrero, Stacking-engineered ferroelectricity in bilayer boron nitride, *Science* **372**, 1458 (2021).

[20] Y. Xie, A. T. Pierce, J. M. Park, D. E. Parker, E. Khalaf, P. Ledwith, Y. Cao, S. H. Lee, S. Chen, P. R. Forrester, *et al.*, Fractional chern insulators in magic-angle twisted bilayer graphene, *Nature* **600**, 439 (2021).

[21] J. M. Park, Y. Cao, K. Watanabe, T. Taniguchi, and P. Jarillo-Herrero, Tunable strongly coupled superconductivity in magic-angle twisted trilayer graphene, *Nature* **590**, 249 (2021).

[22] J. Cai, E. Anderson, C. Wang, X. Zhang, X. Liu, W. Holtzmann, Y. Zhang, F. Fan, T. Taniguchi, K. Watanabe, *et al.*, Signatures of fractional quantum anomalous hall states in twisted MoTe₂, *Nature* **622**, 63 (2023).

[23] Z. Lu, T. Han, Y. Yao, A. P. Reddy, J. Yang, J. Seo, K. Watanabe, T. Taniguchi, L. Fu, and L. Ju, Fractional quantum anomalous hall effect in multilayer graphene, *Nature* **626**, 759 (2024).

[24] Y. Xia, Z. Han, K. Watanabe, T. Taniguchi, J. Shan, and K. F. Mak, Superconductivity in twisted bilayer wse₂, *Nature* **637**, 833 (2025).

[25] Y. Guo, J. Pack, J. Swann, L. Holtzman, M. Cothrine, K. Watanabe, T. Taniguchi, D. G. Mandrus, K. Barmak, J. Hone, *et al.*, Superconductivity in 5.0° twisted bilayer wse₂, *Nature* **637**, 839 (2025).

[26] S. Shallcross, S. Sharma, E. Kandelaki, and O. A. Pankratov, Electronic structure of turbostratic graphene, *Phys. Rev. B* **81**, 165105 (2010).

[27] D. M. Kennes, L. Xian, M. Claassen, and A. Rubio, One-dimensional flat bands in twisted bilayer germanium selenide, *Nature communications* **11**, 1124 (2020).

[28] I. Soltero, J. Guerrero-Sánchez, F. Mireles, and D. A. Ruiz-Tijerina, Moiré band structures of twisted phosphorene bilayers, *Phys. Rev. B* **105**, 235421 (2022).

[29] P. Wang, G. Yu, Y. H. Kwan, Y. Jia, S. Lei, S. Klemenz, F. A. Cevallos, R. Singha, T. Devakul, K. Watanabe, *et al.*, One-dimensional luttinger liquids in a two-dimensional moiré lattice, *Nature* **605**, 57 (2022).

[30] F. Yuan, Y. Jia, G. Cheng, R. Singha, S. Lei, N. Yao, S. Wu, and L. M. Schoop, Atomic resolution imaging of highly air-sensitive monolayer and twisted-bilayer WTe₂, *Nano Letters* **23**, 6868 (2023).

[31] S. J. Magorrian and N. D. Hine, Strain-dependent one-dimensional confinement channels in twisted bilayer 1T'-WTe₂, *Phys. Rev. B* **110**, 045410 (2024).

[32] X. Yang, Y. Zhang, L. Chen, K. Aso, W. Yamamori, R. Moriya, K. Watanabe, T. Taniguchi, T. Sasagawa, N. Nakatsuji, M. Koshino, Y. Yamada-Takamura, Y. Oshima, and T. Machida, Intrinsic one-dimensional moiré superlattice in large-angle twisted bilayer WTe₂, *ACS Nano* **19**, 13007 (2025), pMID: 40145593.

[33] D. An, T. Zhang, Q. Xu, H. Guo, M. U. Rehman, D. M. Kennes, A. Rubio, L. Wang, and L. Xian, Critical angles and one-dimensional moiré physics in twisted rectangular lattices, arXiv preprint arXiv:2507.14435 (2025).

[34] P. Drózdż, M. Gołębowski, and R. Zdyb, Quasi-1d moiré superlattices in self-twisted two-allotropic antimonene heterostructures, *Nanoscale* **16**, 15960 (2024).

[35] D. de Sousa, S. Lee, F. Guinea, and T. Low, Moiré collapse and luttinger liquids in twisted anisotropic homobilayers, arXiv preprint arXiv:2506.19727 (2025).

[36] A. Sinner, P. A. Pantaleón, and F. Guinea, Strain-induced quasi-1d channels in twisted moiré lattices, *Phys. Rev. Lett.* **131**, 166402 (2023).

[37] F. Escudero, A. Sinner, Z. Zhan, P. A. Pantaleón, and F. Guinea, Designing moiré patterns by strain, *Physical Review Research* **6**, 023203 (2024).

[38] N. C. Hesp, S. Batlle-Porro, R. Krishna Kumar, H. Agarwal, D. Barcons Ruiz, H. Herzig Sheinfux, K. Watanabe, T. Taniguchi, P. Stepanov, and F. H. Koppens, Cryogenic nano-imaging of second-order moiré superlattices, *Nature Materials* **23**, 1664 (2024).

[39] F. S. Boi, O. Odunmbaku, A. Taallah, and S. Wang, Quasi-1d, rectangular-like and hexagonal moiré superlattices in exfoliated highly oriented pyrolytic graphite, *Diamond and Related Materials* **151**, 111843 (2025).

[40] L. Su, Y. Gao, Y. Chen, M. U. Farooq, L. Xian, and L. Huang, Domain-selective 1d moiré engineering and topological transitions in bilayer graphene, *Nano Letters* **25**, 14060 (2025).

[41] J. S. Alden, A. W. Tsen, P. Y. Huang, R. Hovden, L. Brown, J. Park, D. A. Muller, and P. L. McEuen, Strain solitons and topological defects in bilayer graphene, *Proceedings of the National Academy of Sciences* **110**, 11256 (2013).

[42] K. Uchida, S. Furuya, J.-I. Iwata, and A. Oshiyama, Atomic corrugation and electron localization due to moiré patterns in twisted bilayer graphenes, *Phys. Rev. B* **90**, 155451 (2014).

[43] P. San-Jose, A. Gutiérrez-Rubio, M. Sturla, and F. Guinea, Electronic structure of spontaneously strained graphene on hexagonal boron nitride, *Phys. Rev. B* **90**, 115152 (2014).

[44] N. N. T. Nam and M. Koshino, Lattice relaxation and energy band modulation in twisted bilayer graphene, *Phys. Rev. B* **96**, 075311 (2017).

[45] F. Guinea and N. R. Walet, Continuum models for twisted bilayer graphene: Effect of lattice deformation and hopping parameters, *Phys. Rev. B* **99**, 205134 (2019).

[46] M. Koshino and N. N. T. Nam, Effective continuum model for relaxed twisted bilayer graphene and moiré electron-phonon interaction, *Phys. Rev. B* **101**, 195425 (2020).

[47] B. Tsim, N. N. T. Nam, and M. Koshino, Perfect one-dimensional chiral states in biased twisted bilayer graphene, *Phys. Rev. B* **101**, 125409 (2020).

[48] Z. Wu, Z. Zhan, and S. Yuan, Lattice relaxation, mirror symmetry and magnetic field effects on ultraflat bands in twisted trilayer graphene, *Science China Physics, Mechanics & Astronomy* **64**, 267811 (2021).

[49] N. Leconte, S. Javvaji, J. An, A. Samudrala, and J. Jung, Relaxation effects in twisted bilayer graphene: A multi-scale approach, *Phys. Rev. B* **106**, 115410 (2022).

[50] X. Qian, J. Liu, L. Fu, and J. Li, Quantum spin hall effect in two-dimensional transition metal dichalcogenides, *Science* **346**, 1344 (2014).

[51] E. Torun, H. Sahin, S. Cahangirov, A. Rubio, and F. Peeters, Anisotropic electronic, mechanical, and optical properties of monolayer WTe₂, *Journal of Applied Physics* **119** (2016).

[52] L. Muechler, A. Alexandradinata, T. Neupert, and R. Car, Topological nonsymmorphic metals from band inversion, *Phys. Rev. X* **6**, 041069 (2016).

[53] F. Zheng, C. Cai, S. Ge, X. Zhang, X. Liu, H. Lu, Y. Zhang, J. Qiu, T. Taniguchi, K. Watanabe, *et al.*, On the quantum spin hall gap of monolayer 1T'-WTe₂, *Advanced Materials* **28**, 4845 (2016).

[54] S. Tang, C. Zhang, D. Wong, Z. Pedramrazi, H.-Z. Tsai, C. Jia, B. Moritz, M. Claassen, H. Ryu, S. Kahn, *et al.*, Quantum spin hall state in monolayer 1T'-WTe₂, *Nature Physics* **13**, 683 (2017).

[55] V. Fatemi, S. Wu, Y. Cao, L. Bretheau, Q. D. Gibson, K. Watanabe, T. Taniguchi, R. J. Cava, and P. Jarillo-Herrero, Electrically tunable low-density superconductivity in a monolayer topological insulator, *Science* **362**, 926 (2018).

[56] S.-Y. Xu, Q. Ma, H. Shen, V. Fatemi, S. Wu, T.-R. Chang, G. Chang, A. M. M. Valdivia, C.-K. Chan, Q. D. Gibson, *et al.*, Electrically switchable berry curvature dipole in the monolayer topological insulator WTe₂, *Nature Physics* **14**, 900 (2018).

[57] J. Yang, Y. Jin, W. Xu, B. Zheng, R. Wang, and H. Xu, Oxidation-induced topological phase transition in monolayer 1T'-WTe₂, *The journal of physical chemistry letters* **9**, 4783 (2018).

[58] Q. Zhang, R. Zhang, J. Chen, W. Shen, C. An, X. Hu, M. Dong, J. Liu, and L. Zhu, Remarkable electronic and optical anisotropy of layered 1t'-WTe₂ 2d materials, *Beilstein Journal of Nanotechnology* **10**, 1745 (2019).

[59] Y. Shi, J. Kahn, B. Niu, Z. Fei, B. Sun, X. Cai, B. A. Francisco, D. Wu, Z.-X. Shen, X. Xu, *et al.*, Imaging quantum spin hall edges in monolayer WTe₂, *Science advances* **5**, eaat8799 (2019).

[60] S. Ok, L. Muechler, D. Di Sante, G. Sangiovanni, R. Thomale, and T. Neupert, Custodial glide symmetry of quantum spin hall edge modes in monolayer wte 2, *Phys. Rev. B* **99**, 121105 (2019).

[61] C. Zhao, M. Hu, J. Qin, B. Xia, C. Liu, S. Wang, D. Guan, Y. Li, H. Zheng, J. Liu, *et al.*, Strain tunable

semimetal-topological-insulator transition in monolayer 1 T'-WTe₂, Phys. Rev. Lett. **125**, 046801 (2020).

[62] W. Zhao, Z. Fei, T. Song, H. K. Choi, T. Palomaki, B. Sun, P. Malinowski, M. A. McGuire, J.-H. Chu, X. Xu, *et al.*, Magnetic proximity and nonreciprocal current switching in a monolayer WTe₂ helical edge, Nature Materials **19**, 503 (2020).

[63] M. Hu, G. Ma, C. Y. Wan, and J. Liu, Realistic tight-binding model for monolayer transition metal dichalcogenides of 1T' structure, Phys. Rev. B **104**, 035156 (2021).

[64] W. Zhao, E. Runburg, Z. Fei, J. Mutch, P. Malinowski, B. Sun, X. Huang, D. Pesin, Y.-T. Cui, X. Xu, *et al.*, Determination of the spin axis in quantum spin hall insulator candidate monolayer WTe₂, Phys. Rev. X **11**, 041034 (2021).

[65] B. Sun, W. Zhao, T. Palomaki, Z. Fei, E. Runburg, P. Malinowski, X. Huang, J. Cenker, Y.-T. Cui, J.-H. Chu, *et al.*, Evidence for equilibrium exciton condensation in monolayer WTe₂, Nature Physics **18**, 94 (2022).

[66] Y. Maximenko, Y. Chang, G. Chen, M. R. Hirsbrunner, W. Swiech, T. L. Hughes, L. K. Wagner, and V. Madhavan, Nanoscale studies of electric field effects on monolayer 1T'-WTe₂, npj Quantum Materials **7**, 29 (2022).

[67] J. Lee, J. Kwon, E. Lee, J. Park, S. Cha, K. Watanabe, T. Taniguchi, M.-H. Jo, and H. Choi, Spinful hinge states in the higher-order topological insulators WTe₂, Nature Communications **14**, 1801 (2023).

[68] L. Watson, J. Ripoll, Z. Tong, A. Kumar, Y. Que, Y.-H. Chan, H. Lin, S. Mukherjee, M. Garnica, M. T. Edmonds, *et al.*, Observation of the charge density wave excitonic order parameter in topological insulator monolayer WTe₂, ACS nano **19**, 32374 (2025).

[69] G. Kresse and J. Furthmüller, Efficiency of ab-initio total energy calculations for metals and semiconductors using a plane-wave basis set, Computational Materials Science **6**, 15 (1996).

[70] G. Kresse and J. Furthmüller, Efficient iterative schemes for ab initio total-energy calculations using a plane-wave basis set, Phys. Rev. B **54**, 11169 (1996).

[71] T. Ozaki, Variationally optimized atomic orbitals for large-scale electronic structures, Phys. Rev. B **67**, 155108 (2003).

[72] T. Ozaki and H. Kino, Numerical atomic basis orbitals from h to kr, Phys. Rev. B **69**, 195113 (2004).

[73] T. Ozaki and H. Kino, Efficient projector expansion for the ab initio lcao method, Phys. Rev. B **72**, 045121 (2005).

[74] J. P. Perdew, K. Burke, and M. Ernzerhof, Generalized gradient approximation made simple, Phys. Rev. Lett. **77**, 3865 (1996).

[75] S. Grimme, J. Antony, S. Ehrlich, and H. Krieg, A consistent and accurate ab initio parametrization of density functional dispersion correction (dft-d) for the 94 elements h-pu, The Journal of Chemical Physics **132**, 10.1063/1.3382344 (2010).

[76] P. E. Blöchl, Projector augmented-wave method, Phys. Rev. B **50**, 17953 (1994).

[77] I. Morrison, D. M. Bylander, and L. Kleinman, Nonlocal hermitian norm-conserving vanderbilt pseudopotential, Phys. Rev. B **47**, 6728 (1993).

[78] H. J. Monkhorst and J. D. Pack, Special points for brillouin-zone integrations, Phys. Rev. B **13**, 5188 (1976).

[79] J. He, K. Hummer, and C. Franchini, Stacking effects on the electronic and optical properties of bilayer transition metal dichalcogenides MoS₂, MoSe₂, WS₂, and WSe₂, Phys. Rev. B **89**, 075409 (2014).

[80] A. Weston, Y. Zou, V. Enaldiev, A. Summerfield, N. Clark, V. Zólyomi, A. Graham, C. Yelgel, S. Magorrian, M. Zhou, *et al.*, Atomic reconstruction in twisted bilayers of transition metal dichalcogenides, Nature nanotechnology **15**, 592 (2020).

[81] W. Zhai, Z. Li, Y. Wang, L. Zhai, Y. Yao, S. Li, L. Wang, H. Yang, B. Chi, J. Liang, *et al.*, Phase engineering of nanomaterials: transition metal dichalcogenides, Chemical Reviews **124**, 4479 (2024).

[82] P. M. Chaikin and T. C. Lubensky, *Principles of Condensed Matter Physics* (Cambridge University Press, Cambridge, 1995).

[83] S. Steiner, S. Khmelevskyi, M. Marsmann, and G. Kresse, Calculation of the magnetic anisotropy with projected-augmented-wave methodology and the case study of disordered Fe_{1-x}Co_x alloys, Phys. Rev. B **93**, 224425 (2016).